The coherent structures of shallow-water turbulence: Deformation-radius effects, cyclone/anticyclone asymmetry and gravity-wave generation

L. M. Polvani
Department of Applied Physics, Columbia University, New York, New York 10027

J. C. McWilliams
National Center for Atmospheric Research, Boulder, Colorado 80307

M. A. Spall
Woods Hole Oceanographic Institution, Woods Hole, Massachusetts 02543

R. Ford[a)]
D.A.M.T.P., University of Cambridge, Silver Street, Cambridge, CB3 9EW, England

(Received 25 January 1994; accepted for publication 8 April 1994)

Over a large range of Rossby and Froude numbers, we investigate the dynamics of initially balanced decaying turbulence in a shallow rotating fluid layer. As in the case of incompressible two-dimensional decaying turbulence, coherent vortex structures spontaneously emerge from the initially random flow. However, owing to the presence of a free surface, a wealth of new phenomena appear in the shallow-water system. The upscale energy cascade, common to strongly rotating flows, is arrested by the presence of a finite Rossby deformation radius. Moreover, in contrast to near-geostrophic dynamics, a strong asymmetry is observed to develop as the Froude number is increased, leading to a clear dominance of anticyclonic vortices over cyclonic ones, even though no β effect is present in the system. Finally, we observe gravity waves to be generated around the vortex structures, and, in the strongest cases, they appear in the form of shocks. We briefly discuss the relevance of this study to the vortices observed in Jupiter's atmosphere.

O plunge your hands in the water,
Plunge them in up to the wrist;
Stare, stare in the basin
And wonder at what you've missed.
-W. H. Auden

I. INTRODUCTION

The dynamics of decaying incompressible two-dimensional turbulence has been the subject of much attention in the last decade.[1] The spontaneous emergence of coherent vortex structures [McWilliams (1984)] and their evolution has been widely investigated, both computationally and theoretically [see, among many others, Santangelo *et al.* (1989); Carnevale *et al.* (1991); Dritschel 1993].

In two-dimensional turbulence, the flow is constrained to strictly horizontal motions and the depth of the fluid layer is constant (i.e., the fluid lies between a rigid lid and rigid bottom); this implies the complete absence of vortex stretching. For atmospheric and oceanic applications this restriction is somewhat severe, and several steps toward more realistic systems have been taken. Larichev and McWilliams (1991) have studied the evolution of turbulence in an "equivalent barotropic" model, and Cushman-Roisin and Tang (1990) in a "generalized geostrophic" model.

While these models can be useful tools for understanding specific phenomena in designated limits of parameter space, they suffer from the limitation of resting upon asymptotic approximations of the underlying primitive equations, for the one layer case the shallow-water equations (hereafter SWE). Under such approximations to the SWE, the flow is constrained to remain within the asymptotic regime defined by these approximations, even if the natural evolution of the flow would tend to move away from that regime, and may eventually evolve through states with Rossby and Froude numbers quite different from their initial values. To avoid this limitation, we study decaying turbulence in the full SWE. Thus, while we initialize the flow in a precise location in parameter space, for instance, with small Rossby and Froude numbers, the evolution is allowed to take place without the constraint of any asymptotic approximations, and the flow evolves freely throughout the full parameter space.

Two previous studies have dealt with turbulence in the SWE. Spall and McWilliams (1992) have analyzed the short-time evolution of initially balanced flows over a large range of Rossby and Froude numbers, and have derived scaling laws for the generation of the unbalanced components of the flow. Farge and Sadourny (1990) have explored the long-time evolution and observed the emergence of coherent vortices for a somewhat restricted set of cases in the regime of small Rossby and Froude numbers, with much attention dedicated to the evolution of the Fourier and wavelet spectra of the flow.

In this paper, we are primarily interested in the physical-space characterization of decaying shallow-water turbulence over the *full* range of Rossby and Froude numbers. In particular, we describe the emergence of coherent structures, the cyclone/anticyclone asymmetry, the evolution of the unbalanced flow, and the generation of gravity waves. Since this study is, to the best of our knowledge, the first exploration of the entire parameter space for long times, our approach in

[a)]Present address: Scripps Institute of Oceanography, 9500 Gilman Drive, La Jolla, California 92093-0225.

 1054-1500/94/4(2)/177/10/$6.00

this paper is primarily phenomenological; hence, most of the discussion will be a quantification of what is actually observed in different domains of parameter space.

The paper is organized as follows. In Sec. II we describe the basics of the problem, with particular attention given to the balanced initialization procedure. In Sec. III, we analyze the emergence of the coherent structures and quantify the evolution of the flow as a function of the parameters of the problem. In Sec. IV, we describe in some detail the cyclone/anticyclone asymmetry, and in Sec. V we quantify the unbalanced motions and the generation of gravity waves. A discussion of how the results of this study may be applicable to Jovian vortices closes the paper in Sec. VI.

II. DEFINITIONS AND BALANCED INITIALIZATION

We start from the dimensional SWE, describing the dynamics of a thin layer of incompressible rotating fluid, confined between a rigid flat bottom and a free surface:

$$\partial_t \mathbf{v}+(\mathbf{v}\cdot\nabla)\mathbf{v}+f_0(\mathbf{k}\times\mathbf{v})=-g\ \nabla h_*,$$

$$\partial_t h_*+\nabla\cdot(h_*\mathbf{v})=0,$$

where $\mathbf{v}$ is the horizontal velocity, h_* is the total height of the fluid column, $\mathbf{k}$ is the unit vector along the axis of rotation, and the other notation is standard. Recall that substitution of a reduced gravity g' in the place of g makes the above set of equations applicable to the upper layer of a two-layer fluid with no free surface and an infinitely deep lower layer at rest; such an *equivalent barotropic* system is more directly of interest for oceanic and Jovian applications.

Given a velocity scale U, a length scale L, and a height scale H, one constructs the Rossby and Froude numbers in the usual way,

$$R=\frac{U}{f_0 L} \quad \text{and} \quad F=\frac{U}{\sqrt{gH}}, \tag{2.1}$$

as ratios between the fluid speed and the rotational and gravitational speeds, respectively. These two numbers define the two-dimensional parameter space of the problem. It is also useful to define the Burger number,

$$B=\frac{R^2}{F^2}=\left(\frac{L_R}{L}\right)^2, \tag{2.2}$$

the square of the ratio of the Rossby deformation radius $L_R=\sqrt{gH}/f_0$ and the typical length scale of the flow. As we will show, the Burger number plays a major role in the emergence of coherent structures from the random initial conditions.

With these definitions, one easily obtains a system of equations for the three nondimensional variables $\mathbf{u}=(u,v)$ and h,

$$R[\partial_t\mathbf{u}+(\mathbf{u}\cdot\nabla)\mathbf{u}]+\mathbf{k}\times\mathbf{u}=-\nabla h, \tag{2.3a}$$

$$RB^{-1}[\partial_t h+\nabla\cdot(h\mathbf{u})]+\nabla\cdot\mathbf{u}=0, \tag{2.3b}$$

where h is the nondimensional perturbation height and is related to the full dimensional height h_* by the relation $h_*=H(1+RB^{-1}h)$. Without loss of generality, this choice of scales immediately brings out in (2.3) the momentum balance and nondivergence of the flow that are expected in the traditional geostrophic limit $R\ll 1$ and $L\approx L_R$ [i.e., $B=O(1)$].

Since this paper is concerned with the evolution of initially balanced flows, i.e., flows such that freely propagating gravity waves have nearly negligible effects on the evolution of vortices, a special procedure is required to prepare balanced initial conditions. We have chosen to solve the Balance Equations [McWilliams (1985)].

Via Helmholtz' theorem, the velocity field is first written as the sum of a rotational and a divergent component:

$$\mathbf{u}\equiv\mathbf{k}\times\nabla\psi+\epsilon\nabla\chi, \tag{2.4}$$

where the streamfunction ψ and the velocity potential χ are nondimensional and $O(1)$. The parameter ϵ quantifies the ratio of the divergent to the rotational component; this ratio is typically small for a balanced flow. McWilliams (1985) has shown that the definition,

$$\epsilon=R\,\frac{\max(1,R)}{\max(1,B)},$$

leads to a uniform definition of balance (i.e., $\epsilon\ll 1$) when either $R\ll 1$ or $F\ll 1$, or both.

Substituting (2.4) into the SWE (2.3), one first constructs the divergence and vorticity equations. Then, combining these two with the continuity equation (2.3b) so as to eliminate all time derivatives, a so-called "omega equation" is derived. Finally, truncation of these three equations so as to eliminate all terms of $O(\epsilon R)$ and smaller leads to the following set of Balance Equations:

$$\nabla^2\psi_t=J(\psi,\nabla^2\psi)+R^{-1}\ \nabla^2\chi+\nabla\cdot(\nabla^2\psi\ \nabla\chi), \tag{2.5a}$$

$$\nabla^2 h=\nabla^2\psi+2RJ(\psi_x,\psi_y), \tag{2.5b}$$

$$\begin{aligned}R^{-1}(1-B\nabla^2)\nabla^2\chi=&-J(\psi,\nabla^2\chi)+\nabla^2 J(\psi,h)\\&+2RJ(\psi_x,\psi_y)_t-\nabla\cdot(\nabla^2\psi\ \nabla\chi)\\&+\nabla^2[\nabla\cdot(h\ \nabla\chi)].\end{aligned} \tag{2.5c}$$

For a detailed derivation, the reader should refer to Spall and McWilliams (1992). These three equations allow us to balance the initially random field as follows.

We start by choosing a kinetic energy spectrum for the rotational part of the flow,

$$E_K(\mathbf{k})\sim\frac{k^{m/2}}{(k+k_0)^m}, \tag{2.6}$$

where $k=|\mathbf{k}|$ and k_0 and m are constants discussed below. The streamfunction is constructed using the relationship

$$\tfrac{1}{2}k^2|\psi_{\mathbf{k}}|^2=E_K(\mathbf{k}),$$

where $\psi_{\mathbf{k}}$ are the Fourier coefficients of the streamfunction ψ. These coefficients are chosen to have random phases, and amplitudes yielding the shape (2.6) for E_K.

Given the streamfunction, we can determine h and χ that solve the Balance Equations (2.5). The height field h is easily obtained by inverting (2.5b), whereas χ has to be found by iteration. Starting with $\chi=0$, χ is determined by solving (2.5c) using the numerical scheme,

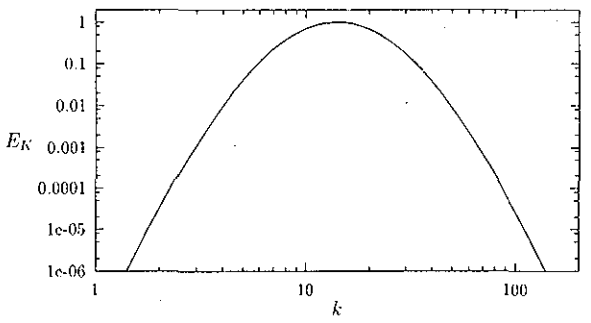

FIG. 1. Initial kinetic energy spectrum.

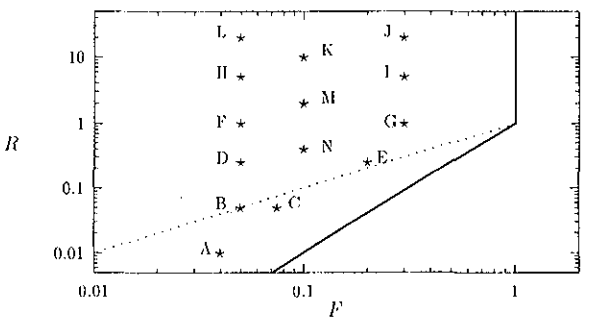

FIG. 2. The (R,F) parameter space, and the location of the runs discussed in this paper (cf. Table I). The dotted line is the line $B=1$, i.e., $L=L_R$. The solid lines roughly indicate the boundary to whose right the SWE cease to apply.

$$R^{-1}(1-B\nabla^2)\nabla^2\{\chi\}^{n+1}=\{-J(\psi,\nabla^2\chi)+\nabla^2J(\psi,h)+2RJ(\psi_x,\psi_y)_t-\nabla\cdot(\nabla^2\psi\,\nabla\chi)+\nabla^2[\nabla\cdot(h\,\nabla\chi)]\}^n,$$

where $\{\}^n$ indicates that the quantity in braces is evaluated at iteration level n.[2] The iteration is repeated until some convergence criterion is satisfied. We have found that this scheme typically converges in a few iterations if we require a relative L_∞ error in χ of order 10^{-6}.

To integrate the SWE (2.3) we have used a pseudospectral scheme for the spatial discretization, with an explicit leapfrog time stepping. As customary, the $\frac{2}{3}$ rule for dealiasing is applied, as well as a ∇^8 hyperviscosity on the right-hand side of (2.3a). Furthermore, a very weak Robert–Asselin filter is applied to the time stepping to suppress the unstable computational mode of the leapfrog scheme [Robert (1966); Asselin (1972)]. Because of limited computer resources and the large number of calculations necessary to cover the (R,F) parameter space and to test dependencies to ensure the robustness of our results, we have performed the runs at a spatial resolution of 200×200. As we will show, this resolution is adequate to capture most of the interesting novel features of this problem; the previous highest resolution long-time integrations were performed at 128×128 [Farge and Sadourny (1990)]. We have repeated a few selected runs at 500×500 and have seen no qualitative difference from the runs at 200×200.

We are interested in clearly observing the upscale energy transfer, and thus we initialize the flow with a narrow spectrum and a reasonably small scale for the kinetic energy centroid. We have used the values $k_0=14$ and $m=25$ in (2.6), for which the shape is illustrated in Fig. 1. Since our resolution is only 200×200, we have refrained from choosing a higher value of k_0 in order to be able to properly resolve the initially small vortices. With our choice of k_0, the energy dissipation is typically of the order of a few percent over very long runs, most of it occurring at very early times when the vortices are small.

Finally, we mention some scaling considerations before presenting the results. In order to explore the dynamics of decaying shallow-water turbulence over the (R,F) parameter space, we need to prepare the initial conditions, such that the flow can be said to be at a given value of R and F. Since Eqs. (2.3) are nondimensional, we choose the initial rms value of u and v equal to $1/\sqrt{2}$ [by setting the proportionality factor in (2.6)], so that the nondimensional rms speed of the initial flow is 1. Similarly, we need the typical initial nondimensional length scale to be 1; this is accomplished by choosing the size of the domain to be $2\pi k_0$. With this scaling, the typical eddy turnover time scale is also equal to 1.

III. COHERENT STRUCTURE FORMATION

The runs we have performed are presented in Fig. 2, where their relative position in the (R,F) parameter space is illustrated. The numerical values of R, F, and B for the runs in Fig. 2 are given in Table I. Also shown is the ratio of the rms values of χ and ψ at $t=0$; this gives an indication of the degree of balance. For easy reference, we have labeled each run by a different letter. In order to allow for meaningful comparisons, all the numerical parameters (resolution, hyperviscosity, Robert–Asselin filter coefficient, etc.) are identical from one run to the next. Only the time step has been varied according to the CFL condition, which is determined by the values of R and F. All runs were integrated from $t=0$ to $t=1000$; because of our scaling, this is equivalent to 1000 eddy turnover times.

It can be seen in Fig. 2 that, while we have been able to explore more than three orders of magnitude in R, the range

TABLE I. Values of R and F and B for the runs in Fig. 2.

Label	R	F	B	$\chi_{\rm rms}/\psi_{\rm rms}$
A	0.01	0.04	0.0625	2.71×10^{-3}
B	0.05	0.05	1.0	8.99×10^{-3}
C	0.05	0.075	0.444	1.08×10^{-2}
D	0.25	0.05	25	1.34×10^{-2}
E	0.25	0.20	1.5625	3.97×10^{-2}
F	1.00	0.05	400	1.06×10^{-2}
G	1.00	0.30	11.11	5.81×10^{-2}
H	5.00	0.05	10 000	5.90×10^{-3}
I	5.00	0.30	278	1.34×10^{-1}
J	20.00	0.30	4444.4	1.65×10^{-1}
K	10.00	0.10	10 000	2.08×10^{-2}
L	20.00	0.05	160 000	5.03×10^{-3}
M	2.0	0.10	400	2.56×10^{-2}
N	0.40	0.10	16	2.70×10^{-2}

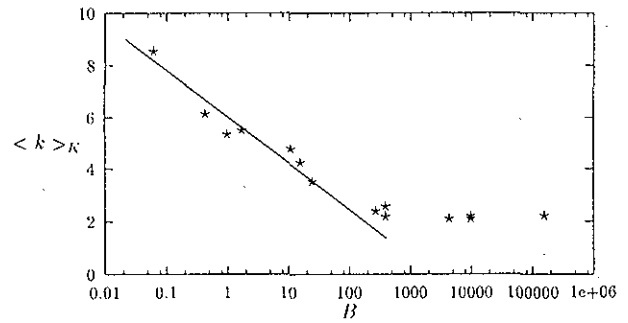

FIG. 3. The centroid of kinetic energy vs B after 1000 eddy turnover times.

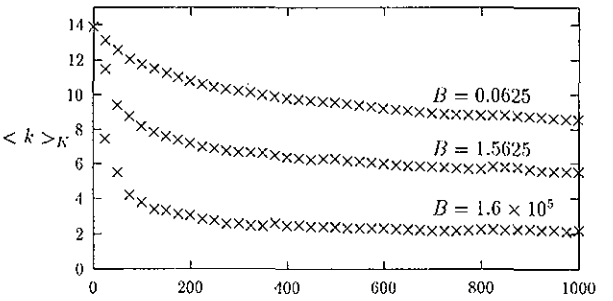

FIG. 4. The centroid of kinetic energy vs time for runs A, E, and L (cf. Table I).

in F is considerably smaller, owing to the following reasons. On the $F \ll 1$ side, the presence of very fast gravity waves forces the time step to become exceedingly small, and hence the computations become prohibitively costly, especially because we need to integrate for very long times to describe the coherent structure formation.

At the other end, i.e., for $F = O(1)$, the SWE cease to be valid. This is due to the fact that the variations in height necessary to produce pressure gradients able to balance the Coriolis force become comparable to the height of the fluid layer. In other words, the thickness $h*$ of the fluid layer tends to go to zero for strong vortices. Simple scaling suggests that for $R > 1$ the boundary is at $F = O(1)$, while for $R \ll 1$ it is located around $R = O(F^2)$. These indicative boundaries are shown by the solid lines in Fig. 2. In practice, we do not know *a priori* whether a given initial condition will lead to $h*$ going to zero somewhere in the domain; we have simply tried to choose as large a value of F as possible for each value of R; when the evolution has led to $h* = 0$, we have restarted the run at smaller F. A careful analysis of this problem has recently been performed by Yavneh and McWilliams (1993b).

A first robust result emerging from these runs is that the formation of coherent structures from the initially random field is primarily controlled by the Burger number B, i.e., by how the average initial vortex size compares to the deformation radius. A first indication of this is given in Fig. 3, where we have plotted the centroid of kinetic energy $\langle k \rangle_K$ at $t = 1000$ versus the value of B at $t = 0$ for all the runs in Table I. This centroid is defined by

$$\langle k \rangle_K = \frac{\Sigma_{\mathbf{k}} k(|u_{\mathbf{k}}|^2 + |v_{\mathbf{k}}|^2)}{\Sigma_{\mathbf{k}}(|u_{\mathbf{k}}|^2 + |v_{\mathbf{k}}|^2)},$$

where $u_{\mathbf{k}}$ and $v_{\mathbf{k}}$ are the Fourier coefficients of the variables u and v. Recall that the initial value of this centroid is $\langle k \rangle_K (t = 0) = k_0 = 14$.

When B is small, i.e., when the vortices are initially large compared to the Rossby deformation radius L_R, the inverse cascade is very minor. The smallest value of B we have been able to achieve is for run A, for which $B = 0.0625$; in this case, the kinetic energy centroid has decreased by a factor of about 1.6 over 1000 eddy turnover times, indicating that vortices have only grown in size by about that factor.

We have not performed runs for smaller values of B. From Fig. 2 it should be clear why it is difficult to compute at $B \ll 1$. The dotted line in that figure is the line $B = 1$. The small values of B are cornered in a small region of parameter space bounded by low Froude numbers on one side and the region where $h*$ vanishes on the other (this is the wedge between the dotted and the solid line in Fig. 2).

In the regime $B \ll 1$, the vortices are interacting very weakly. From animation of the vorticity (or the potential vorticity) field, it is actually quite clear that the vortices are barely moving relative to each other, and only feel the influence of the few nearest neighbors. This kind of behavior is reminiscent of the one found in the equivalent-barotropic model studied by Larichev and McWilliams (1991) (the parameter λ in that paper is related to the Burger number via $B = \lambda^{-2}$). In that model, point vortices are known to interact with exponentially decaying strength proportional to $e^{-\lambda r}$ [see also Polvani *et al.* (1989)].

As B is increased, the inverse cascade is able to proceed further, in an approximately logarithmic relation to B, as is attested by the left portion of Fig. 3. A clear break is observed for $B > 100$, and for larger B the curve remains flat. The reason for this behavior is easily explained. With reference to the definitions (2.1) and (2.2), it should be clear that, although we start the calculations at given values of R and F, these numbers change as the turbulence decays because vortex size L increases as a reflection of the inverse energy cascade.

However, the deformation radius is defined by $L_R = \sqrt{gH}/f$, and, since it is independent of L, it remains fixed during the evolution; also fixed is the size of the domain. Because of our choice $k_0 = 14$, it turns out that $B \sim 200$ at $t = 0$ corresponds, in fact, to the case when L_R is equal to the size of the domain. Hence the right (flat) portion of the data in Fig. 3 is associated with those runs for which the deformation radius is comparable to or greater than the size of our domain; the cascade is then controlled by the domain size instead of the deformation radius. We could have chosen a larger value of k_0 to explore the effects at larger initial B, but that would have meant substantially increasing the dissipation.

Figure 4 shows the time evolution of the kinetic energy centroid for runs A, E, and L, which comprise a representative set of B values (cf. Table I). For $B \gg 1$, the cascade is

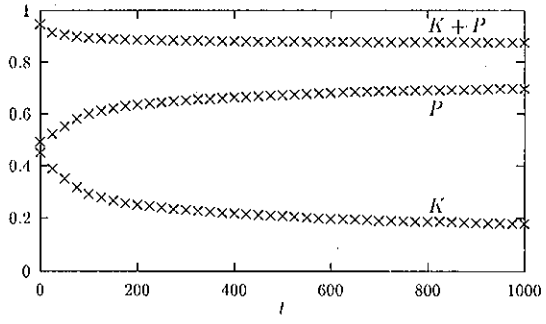

FIG. 5. Kinetic to potential energy conversion during the emergence of coherent structures. Run E, with $R=0.25$ and $F=0.20$.

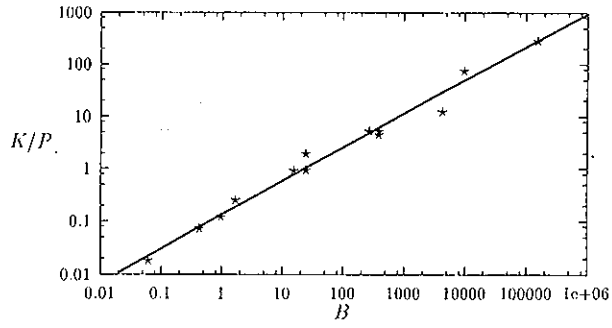

FIG. 6. Kinetic to potential energy ratio vs B for the runs in Table I.

very violent, and in less than 100 eddy turnover times the flow has evolved into just a few vortices that are strongly interacting and advecting each other around the domain; this behavior is, of course, reminiscent of the two-dimensional case, which corresponds precisely to the limit $B\to\infty$.

The emergence of coherent vortices and the associated inverse energy cascade is further clearly illustrated by the conversion of energy from kinetic to potential during the formation of coherent structures. We define the nondimensional kinetic and potential energy as follows:

$$K=\frac{1}{2}\int\int \eta(u^2+v^2)dx\ dy$$

and

$$P=\frac{1}{2F^2}\int\int (\eta^2-1)dx\ dy,$$

where $\eta\equiv h*/H=(1+RB^{-1}h)$ is the total nondimensional height of the fluid layer. The potential energy is defined so that it is zero in the absence of motion, in which case $\eta=1$ everywhere in the domain.

A clear example of the kinetic to potential energy conversion is illustrated in Fig. 5. The total energy $K+P$, which is slightly dissipated at early times, remains virtually constant after $t=100$. In contrast, K and P are rapidly exchanged in the interval $0<t<200$, which corresponds to the time when the coherent structures are formed (cf. the middle curve in Fig. 4). At around $t=200$, the coherent structures have reached a size comparable to the deformation radius, and the inverse cascade is thus severely slowed down, as is manifested by the fact that the values of K and P change much more slowly.

It is interesting to plot the ratio K/P at $t=1000$ as a function of B; this is shown in Fig. 6. Whereas at $t=0$ the points do not fall on a straight line, the evolution adjusts itself so that $K/P\sim B^{\mu}$. We have fitted the points to a line and found $\mu=0.64$.

One last way of quantifying the coherent structures or, more precisely, the intermittency of the flow, is to compute the kurtosis of the vorticity field, defined by

$$\mathrm{Ku}(\zeta)\equiv\frac{\int\int\zeta^4\ dx\ dy}{(\int\int\zeta^2\ dx\ dy)^2},\qquad(3.1)$$

where $\zeta=\nabla^2\psi$. This quantity was first used by McWilliams (1984) to describe the intermittency produced by the emergence of coherent vortices in two-dimensional turbulence.

In the kurtosis plots the contrast between small and large B is quite remarkable. Figure 7 shows the evolution of $\mathrm{Ku}(\zeta)$ for the three runs A, D, and F, representing a small, an intermediate, and a large initial value of B. For run A, the initial vortices are already many times larger than the deformation radius L_R. Thus, over 1000 eddy turnover times, the kurtosis changes very little, from an initial value near 3 associated with the random initial conditions to a final value of about 5.

On the contrary, for run D the initial size of the vortices is approximately $L_R/2$. This allows them to rapidly grow to a size of about L_R by $t=200$ or so. Thereafter, the inverse cascade is arrested and the kurtosis grows little from $t=200$ to $t=1000$. Furthermore, it should be noted that while the kurtosis of vorticity grows from an initial value of 3 to a final value of about 23.5, the kurtosis of streamfunction changes only from 3 to 5 over the same interval of 1000 eddy turnover times.

Finally, the curve associated with run F shows what occurs when the vortices are 20 times smaller than L_R at $t=0$. Since even at the end of the run the vortices are considerably smaller than the deformation radius, the kurtosis continually increases throughout the run. It is interesting to note the jumpiness of the vorticity kurtosis for this run F, especially after $t=600$; it is, in fact, directly correlated with merging

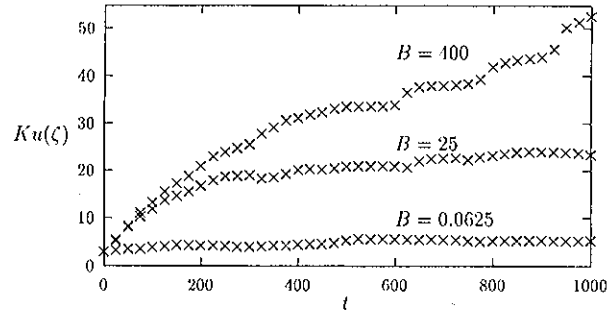

FIG. 7. The kurtosis of vorticity vs time, for the three runs A, D, and F (cf. Table I).

events. Since few vortices are present in the flow at later times, each vortex merger greatly contributes to the increase in the kurtosis.

We conclude this section by showing the pictures of the vorticity fields for the runs we have been discussing. In Fig. 8(a) (Plate 1) the vorticity field at $t=0$ is given; Figs. 8(b)–8(d) (Plate 1) illustrate the vorticity field at $t=1000$ for runs A, B, and D, corresponding to initial values of L equal to $4L_R$, L_R, and $L_R/5$, respectively. Notice that in the case where the vortices are larger than the deformation radius [Fig. 8(b) (Plate 1)], not only do the vortices grow very little in size because merging fails to occur, but they are also much less axisymmetric, more closely packed, and evolve very slowly; such behavior has been observed in the equivalent barotropic model in a number of contexts [Polvani *et al.* (1989); Larichev and McWilliams (1991)].

IV. CYCLONE/ANTICYCLONE ASYMMETRY

A second effect that clearly distinguishes shallow-water turbulence from two-dimensional turbulence is the breakdown of symmetry between cyclones and anticyclones. This asymmetry has been investigated in a number of studies before this one [Charney and Flierl (1981); Williams and Yamagata (1984); Cushman-Roisin and Tang (1990)]. All of these, however, have dealt with asymptotic approximations of the SWE, and have most often included the further complication of the effect of a latitudinally varying rotation (the β effect), hence rendering the cause of the asymmetry often difficult to pinpoint.

One important novel result of this study is the following: as coherent structures emerge from an initially random turbulent shallow-water flow, the anticyclonic vortices are favored over the cyclonic ones; this asymmetry is enhanced by a larger Froude number. We emphasize that the physics of our system does not include a β plane. The often-suggested reason for the asymmetry, i.e., Rossby wave radiation, is therefore nugatory for our system. Our result has been independently confirmed using a different numerical technique by Yavneh and McWilliams (1993a). We now proceed to a quantification.

One first measure of the asymmetry is provided by the skewness of vorticity, defined by

$$S(\zeta)\equiv \frac{\int\int \zeta^3\, dx\, dy}{(\int\int \zeta^2\, dx\, dy)^{3/2}}\,. \tag{4.1}$$

This quantity is zero at $t=0$ since we are initializing the flow with an equal number of positive and negative vortices. In Fig. 9 we plot the evolution of $S(\zeta)$ for the runs F and G, both are at $R=1$, and differ in the Froude number ($F=0.05$ and 0.3, respectively). It is quite clear that at larger F the asymmetry in favor of anticyclonic vorticity is much stronger than at smaller F. It should also be noted that the asymmetry seems to emerge quite early and continue throughout the formation of coherent structures.

That figure is representative of the interesting result that the asymmetry seems to be controlled almost exclusively by the Froude number. To see this, we have plotted in Fig. 10 the value of $S(\zeta)$ at $t=1000$ for all the runs in Fig. 2. We

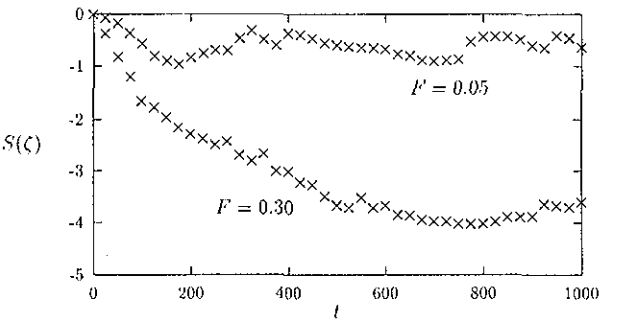

FIG. 9. The skewness of vorticity vs time, for runs F and G.

find that, with the single exception of run A (which is at $B\ll 1$), this quantity is always negative and increases in value with F. The influence of R on the skewness seems quite small, and smaller at smaller F. For instance, at small F the skewness changes relatively little over several orders of magnitude in R (consider the five points at $F=0.05$ in Fig. 10). We have fitted a straight line to the data points in Fig. 10 and find a slope of -10.23.

Another way of quantifying the asymmetry is to compute the probability density function (pdf) of the vorticity field. In Fig. 11(a), we plot it for run B at $t=0$ (dotted line) and $t=1000$ (solid line). The parameter setting here is the traditional geostrophic one, i.e., $R\ll 1$ and $B=O(1)$. Notice how the pdf goes from a Gaussian (the random initial conditions) to an exponential shape; such exponential shapes are typical of intermittent high Reynolds number turbulence.

Furthermore, notice that the tails of the pdf in Fig. 11(a) are essentially symmetric about the origin, which is expected for the quasigeostrophic limit in which run B lies. In contrast, Fig. 11(b) shows the pdf of ζ for run G, for which $R=1.0$ and $F=0.3$. A clear asymmetry is present favoring anticyclonic vorticity at the larger values, pointing to the fact that most of the coherent structures are associated with negative vorticity.

For the reader who may be concerned as to why we are not using the potential vorticity as a diagnostic of asymmetry, we point out that, owing to the initialization procedure we have used, the potential vorticity field in our calculations

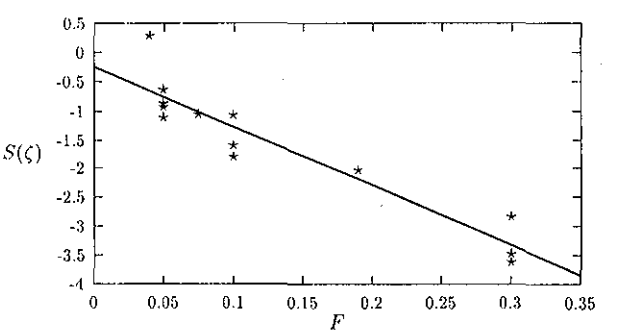

FIG. 10. The skewness of vorticity vs F at $t=1000$ for the runs in Table I.

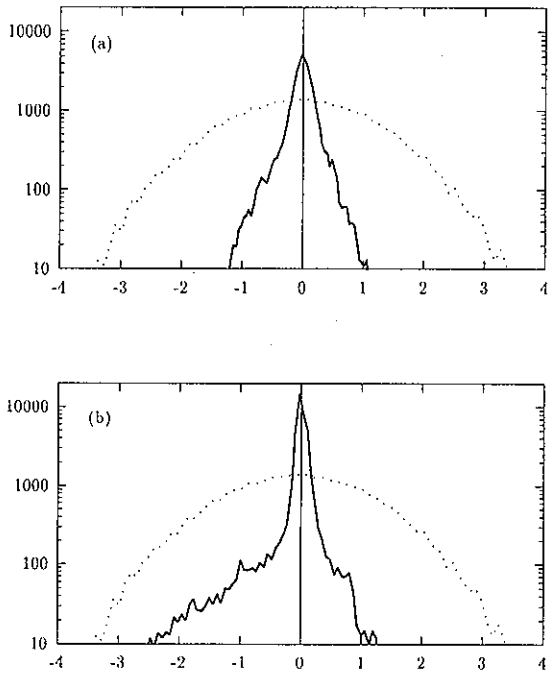

FIG. 11. Probability density functions of vorticity for runs (a) B and (b) G. The dotted lines are initial conditions; the solid lines are at $t=1000$.

is not symmetric at $t=0$, whereas the vorticity is. The symmetry in the pdf of vorticity is a result of the constraint of zero net circulation in the doubly periodic domain. The nonlinear inversion relationship between vorticity and potential vorticity implies that the pdf of potential vorticity will not necessarily be symmetric, even if the pdf of vorticity is. For this reason, the vorticity turns out to be the proper quantity for diagnosing the development of cyclone/anticyclone asymmetry in the present context.

The key issue here is: why are anticyclones favored over cyclones? We do not yet possess an entirely satisfactory quantitative answer to this question, but we would like to illustrate some features we have observed in the evolution of the flow that may point in the right direction. In a previous study with intermediate models [Cushman-Roisin and Tang (1990)], it has been argued that cyclones simply fall apart by themselves, whereas anticyclones are robust. We find that, on the contrary, several large cyclonic structures do emerge in our calculations, even in the cases where a very large asymmetry is present. Also, over the entire (R,F) parameter space we have found no instances of large cyclonic vortices simply falling apart, and suspect that the results of Cushman-Roisin and Tang (1990) may be due to the limitations of the physical model they were studying. Indeed, Ford (1993) has shown that typical growth rates for instabilities of isolated cyclones with a monotonic potential vorticity profile seldom exceed 10^{-4} inverse turnover times throughout the entire (R,F) parameter space.

What we observe in our calculations is that cyclonic vortices are simply not able to grow as fast as anticyclonic ones and retain their coherence. In fact, the asymmetry can be observed rather early, as illustrated in Fig. 12(a) (Plate 2) which shows the vorticity field for run G after only 100 eddy turnover times. Not only are the anticyclonic vortices (blue) already larger in size, but they are also more coherent and axisymmetric. The cyclonic vorticity (red), on the other hand, seems rather disorganized; there are some cyclonic vortices present, but they are smaller in size, and many of them are far from axisymmetric, while large regions of strong cyclonic vorticity appear to be very distorted. A plausible argument for the relative difficulty of cyclonic vortices to grow larger is that since cyclones correspond to contractions of the fluid layer, i.e., $h<0$, the local value of L_R is smaller than for an anticyclone of similar size. This would translate into the fact that the "field of influence" of cyclones is smaller than for anticyclones; the latter would then be more strongly interacting and hence grow faster though repeated mergers.

A second argument for the dominance of anticyclones over cyclones is that the anticyclones are internally more coherent features than cyclones of equal size. To see this, first note that the appropriate range of interaction *within* the cyclone or anticyclone is given by the dimensional quantity $[Q(f_0+v/r)/g]^{-1/2}$, where Q is the potential vorticity and v the dimensional azimuthal velocity.[3] Thus, the range of interaction within each vortex is larger for anticyclones than for cyclones of comparable relative vorticity. It becomes infinite for an anticyclone with zero potential vorticity, and one expects strong internal coherence of the vortex in this limit. On the other hand, in the limit of a very small internal range of interaction, the flow within a vortex appears locally parallel, and the intense vortical nature of the flow is lost; this is precisely the case for cyclonic vortices.

A concluding example is provided by the sequence of Figs. 12(b)–12(d) (Plate 2) showing the vorticity field for run G at $t=425$, 450, and 475. Notice first that the field is clearly dominated by strong coherent nearly axisymmetric anticyclonic vortices (blue), while the few strong cyclonic vortices (red) are very elliptical. In Fig. 12(b) (Plate 2), four vortices can be seen in the left middle portion of the domain; two large anticyclonic vortices, and two smaller cyclonic ones. In the next frame [Fig. 12(c)] (Plate 2), while the two anticyclonic vortices are merging in the familiar way, it becomes clear that the cyclonic vorticity (red) is behaving not unlike a passive tracer, being entrained in the merger of the two anticyclonic vortices. In the last frame [Fig. 12(d)] (Plate 2), one can see the final result of the interaction; the anticyclonic vortices have formed one single larger structure, whereas the cyclonic vorticity is still composed of two small vortices comparable in size to their initial counterparts.

V. GRAVITY-WAVE GENERATION

In this last section we turn our attention to the nonvortical part of the flow, which manifests itself as unbalanced motion and gravity waves. As is well known, this component of the dynamics is very sensitive to the computational scheme used; see, for instance, Farge (1987) and Yuan (1993). We have performed a number of tests to ensure the robustness of the results we present here. In particular, we have found that the unbalanced components of the flow are very sensitive to the value of the Robert–Asselin filter coef-

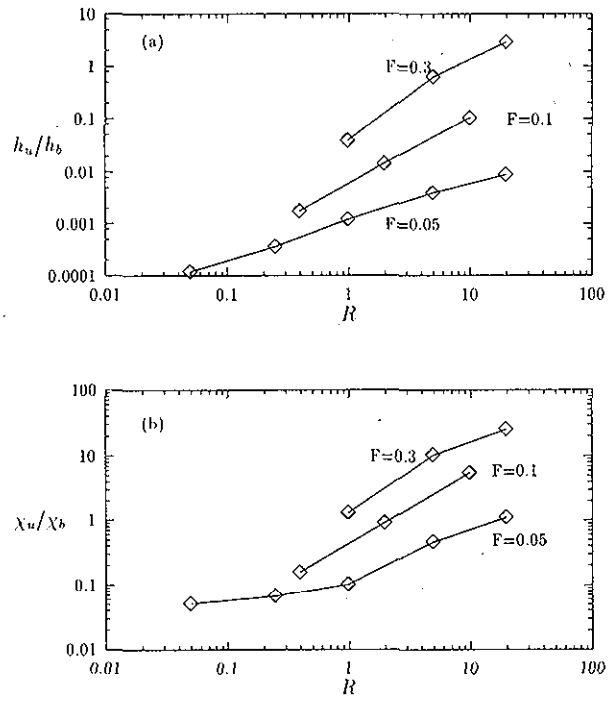

FIG. 13. The ratio of the rms values of unbalanced to balanced (a) h and (b) χ, averaged between $t=500$ and $t=1000$.

ficient α, which is required by the leapfrog scheme to suppress its unstable computational mode. We have therefore repeated many runs with a third-order Adams–Bashforth scheme, which does not possess an unstable computational mode and thus does not require a Robert–Asselin filter [Durran (1991)]. We have found that, with the exception of the $B \ll 1$ regime, a leapfrog scheme with a filter value $\alpha=0.001$ or less gives good agreement with the third-order Adams–Bashforth scheme.

A first quantitative measure of the unbalanced motions is shown in Fig. 13. At each time step we compute the balanced height and velocity potential, h_b and χ_b respectively, by solving the Balance Equations (2.5) from the full streamfunction ψ. The unbalanced fields are then defined by the relationships $h_u \equiv h - h_b$ and $\chi_u \equiv \chi - \chi_b$. To obtain a representative magnitude of the unbalanced motion, we compute the rms values over the entire domain, we normalize the unbalanced fields by their balanced counterparts, and we average from $t=500$ to $t=1000$ in order to exclude the initial adjustment period. The ratios h_u/h_b and χ_u/χ_b are plotted in Fig. 13 versus R for several values of F.

The result emerging from Fig. 13 is that the unbalanced motion increases with R, and is larger at larger F. This is consistent with the scalings found by Spall and McWilliams (1992). The unbalanced amplitudes at $R \gg 1$ are close to what they found in relatively short-time integrations, and are consistent with predictions based on a multiscale asymptotic scaling estimate, which is appropriate for an unbalanced field dominated by gravity waves [cf. Eq. (25) and Fig. 11 in Spall and McWilliams (1992)]. The unbalanced amplitudes are much larger than would be consistent with the single-scale estimate based on an unbalanced field, which is dominated by rotational motion [cf. their Eq. (24)].

In contrast to the results of Spall and McWilliams, the unbalanced amplitudes at $R \ll 1$ in Fig. 13 appear to also be consistent with the assumption that the unbalanced motion is dominated by gravity waves. In the asymptotic limit of $F \ll 1$ and $R \ll 1$, the multiscale estimate for the unbalanced amplitude is $\chi_u/\chi_b = O(F)$. This behavior is evident in Fig. 13 for $F=0.05$, where the unbalanced amplitude is approaching 0.05 as R becomes small. Spall and McWilliams (1992), on the other hand, found that the unbalanced amplitude at $R \ll 1$ was of $O(R^2)$, consistent with the single-scale theory and much smaller than that predicted by the multiscale theory (their Fig. 8). This discrepancy may be due to either the much longer integration times in the present study (it may take longer for the rotational motion to force the gravity waves when $R \ll 1$) or, perhaps, to the fact that the runs performed here are considerably less dissipative than the ones of Spall and McWilliams.

A complementary way of quantifying the unbalanced component of the flow is to apply to the SWE the formalism of Lighthill's theory of sound wave generation by turbulence. The acoustic waves in two-dimensional compressible gas dynamics are the analogs of the gravity waves in the SWE, and the Mach number is the analog of the Froude number. Following Lighthill (1952), the key idea is then to manipulate the SWE in such a way as to obtain a linear wave operator on the left-hand side of an equation and then consider the terms on the right-hand side as forcing terms that generate gravity waves. A full derivation of this is already in the literature, and we therefore limit ourselves here to stating the results, referring the reader to Ford (1993) for details.

Taking various combinations of time and space derivatives of the SWE (2.3), one constructs the following Lighthill equation:

$$(\partial_t^2 + R^{-2} - F^{-2}\nabla^2)\partial_t h = \partial_i \partial_j T_{ij}, \tag{5.1}$$

where the indices i and j are implicitly contracted on the right-hand side. The Lighthill tensor T_{ij} is defined by

$$T_{ij} = \partial_t(hu_i u_j) + (1/2R)(\epsilon_{ik} h u_j u_k + \epsilon_{jk} h u_i u_k) + (1/R)\,\delta_{ij}\, h\, \partial_t h, \tag{5.2}$$

where ϵ_{ij} is the Levi-Civita tensor of rank two,[4] and δ_{ij} is Kronecker's delta. The forcing term $\partial_i \partial_j T_{ij}$ on the left-hand side of (5.1) is then a source gravity waves.

This term is plotted in Fig. 14(a) (Plate 3) for frame $t=500$ of run F ($R=1$, $F=0.05$); it should be compared with the corresponding vorticity field in Fig. 14(b) (Plate 3). Three key points emerge from that figure. First, $\partial_i \partial_j T_{ij}$ is highly correlated with the location of the coherent structures. Second, it is clear that $\partial_i \partial_j T_{ij}$ appears to be mostly of dipolar form, while the vortices are monopolar. Third, $\partial_i \partial_j T_{ij}$ is much larger in the vicinity of cyclones than anticyclones. The first point simply confirms that vortices are the predominant sources of gravity waves. The second and third points require explanation.

For a single isolated vortex, $\partial_i \partial_j T_{ij}$ must be quadrupolar, and thus the dipoles in Fig. 14(a) (Plate 3) are at first sight

surprising; it can, however, be shown that dipoles are the direct result of the mutual advection. An important component of the Lighthill theory at small Froude number is that the integrated effect of vortical motions is to give rise to a quadrupolar radiated sound field. This remains true in our case: although each vortex individually makes a dipolar contribution to $\partial_i \partial_j T_{ij}$, the integrated dipole term is zero.

As for the third point, the nature of the asymmetry in the $\partial_i \partial_j T_{ij}$ field between cyclones and anticyclones may seem surprising, in view of the fact that anticyclones are more vigorous than cyclones, and may therefore be expected to contribute more to the Lighthill source term. However, being internally robust, the anticyclones are essentially axisymmetric. By contrast, the cyclones are less robust and become substantially deformed, and thus yield a larger contribution to the Lighthill source term.

The Lighthill approach is informative at small F because the gravity wave amplitudes remain small at all times, and the scale of the vortical flow is small compared with the scale of the gravity waves that it generates. At large F, the situation is quite different, and the assumption of linearity and the scale separation break down. What we observe in that regime is the formation of shocks, more precisely, *bores* in the present context of an incompressible fluid with a free surface. These are of sufficiently large amplitude that they can be seen directly in the height field. An example is given in Fig. 15 (Plate 4) where the height and vorticity fields are plotted in (a) and (b), respectively for run I at $t=1000$.

Of particular interest in that figure is the fact that large coherent vortex structures are literally surrounded by a "soup" of nonlinear gravity wave bores, of which the vorticity field shows no trace. It is unclear for the moment how the bores are precisely generated, but we have observed them for a variety of different numerical parameter values (hyperviscosity, time step, etc.), and with two different time integration schemes (leapfrog and Adams–Bashforth). They have also been independently observed in the study by Ford (1993). We therefore believe them to be real (and not numerical artifacts), although our resolution is probably inadequate to compute them accurately.

One robust feature we have observed is that near the strongest vortices [cf. the strong anticyclone in the upper-left quadrant of Fig. 15(a)] (Plate 4) the bores seem to emerge radially out of the vortex cores. This is very reminiscent of the situation for compressible two-dimensional flows, specifically of the "shocklets" that have been observed by Chan *et al.* (1993) during the instability of compressible two-dimensional vortices (for instance, in their Figs. 13 and 14). By analogy, these nonlinear gravity waves may be referred to with the term "borelets," i.e., bores of finite extent.

We have observed borelets to form almost every time a pairing occurs between a cyclone and an anticyclone. These appear in the form of a "bridge" between a cyclonic and an anticyclonic vortex; a very clear one can be observed in the upper-left quadrant of Fig. 15(a) (Plate 4). The formation of shocklets within a vortex dipole has also been observed in the compressible two-dimensional context [Scheidegger *et al.* (1993)]. Here we have the shallow-water analog.

VI. DISCUSSION

Owing to the presence of a free surface that allows for vortex stretching, the dynamics of decaying turbulence in a shallow-water rotating fluid is considerably richer than its nondivergent two-dimensional counterpart. Three features, in particular, have emerged from the present study, the first to span the entire Rossby–Froude parameter space for long integration times.

In the first place, whereas in two-dimensional Euler decaying turbulence the flow has no intrinsic physical length scale associated with it, a rotating shallow-water system possesses a finite Rossby deformation radius L_R; this property makes it a much more appealing candidate for realistic geophysical situations. We have found that L_R plays a crucial role in controlling the inverse cascade and thus determining the size of the coherent structures. Essentially, after the vortices have grown to a size comparable to L_R, they interact only weakly, and the inverse cascade is severely arrested.

Second, the symmetry between cyclonic and anticyclonic vortices, found in both two-dimensional Euler and quasigeostrophic systems, is absent from the shallow-water system. We have found that anticyclonic vortices are generally preferred, especially at large F. One particularly interesting application of this may be to the atmosphere of Jupiter, where over 90% of the vortices are observed to be anticyclonic [MacLow and Ingersoll (1986)]. The asymmetry has often been argued to result from the fact that a KdV-type balance between dispersive Rossby waves and nonlinearity can only be achieved for anticyclones [see, for instance, Nezlin and Snezhkin (1993)]. However, the majority of Jovian vortices are actually quite small compared to Jupiter's radius, and hence Rossby wave dispersion due to the β effect may not be strong enough to explain the asymmetry.

In the present study with the SWE, we have found that anticyclonic vortices are strongly favored at larger Froude number. Choosing standard values[5] of $gH=10^{-5}$ ms^{-2} and $U=100$ ms^{-1}, yields $F=0.32$. A value of $U=50$ ms^{-1} is perhaps more appropriate for most of the higher latitude Jovian jets, and this gives $F=0.16$. As can be seen from Fig. 10, these values compare favorably with those we have found, to give the largest asymmetry. The point we wish to make here is that ageostrophic effects may be as important as the β effect in generating the cyclone/anticyclone asymmetry.

Third, we have observed large-amplitude gravity wave bores being generated in the vicinity of and coexisting with large coherent vortices, with a remarkable degree of similarity with what is being found in compressible two-dimensional vortex dynamics [also see Ford (1993)].

In many ways, the richness of decaying turbulence in the SWE that we have uncovered in this study really motivates the study of a number of simpler fundamental processes. Among the outstanding problems we are currently pursuing, the questions of wave/vortex and vortex/vortex interactions seem of greatest importance. We hope to report on them in a future paper.

ACKNOWLEDGMENTS

The original derivation of the Lighthill theory as applied to the SWE is due to Dr. Warwick Norton (unpublished). LMP wishes to thank the members of Climate and Global Dynamics Division for their hospitality during his visit to NCAR. The computations were performed on the NCAR Cray; NCAR is sponsored by the National Science Foundation. MAS has been supported by Grant No. OCE-9301323 and LMP, in part, by Grant No. ATM-90-20999, both from the National Science Foundation.

[1]In the atmospheric and oceanic science communities the term "two-dimensional incompressible" is usually substituted with the expression "barotropic nondivergent on the f plane." The two are identical, since they both solve the two-dimensional Euler equations.

[2]At each step in the iteration, the term $J(\psi_x,\psi_y)_t$ is evaluated by inverting (2.5a) for ψ_t and using the expression $J(\psi_x,\psi_y)_t=(\psi_t)_{xx}\psi_{yy}+\psi_{xx}(\psi_t)_{yy}-2\psi_{xy}(\psi_t)_{xy}$.

[3]This result is obtained by combining cyclostrophic balance and the definition of potential vorticity into a single second-order differential equation for the azimuthal velocity for an axisymmetric vortex. This equation is the shallow-water analog of Eq. (29) of Hoskins *et al.* (1985). Our expression for $f_{loc}=f_0+v/r$ differs slightly from theirs, owing to the fact that an extra differentiation is required in their case to eliminate the Montgomery potential.

[4]Explicitly, $\epsilon_{11}=\epsilon_{22}=0$, and $\epsilon_{12}-\epsilon_{21}=1$.

[5]For the Jovian atmosphere, Williams and Wilson (1988) have used $gH=2.64\times10^{-5}$ ms^{-2}, while Dowling and Ingersoll (1989) have preferred $gH=0.96\times10^{-5}$ ms^{-2}.

Asselin, R., "Frequency filter for time integrations," Mon. Weather Rev. **100**, 487–490 (1972).

Carnevale, G. F., J. C. McWilliams, Y. Pomeau, J. B. Weiss, and W. R. Young, "Evolution of vortex statistics in two-dimensional turbulence," Phys. Rev. Lett. **66**, 2735–2737 (1991).

Cushman-Roisin, B. and B. Tang, "Geostrophic turbulence and emergence of eddies beyond the radius of deformation," J. Phys. Ocean. **20**, 97–113 (1990).

Chan, W. M., K. Shariff, and T. H. Pulliam, "Instabilities of two-dimensional inviscid incompressible vortices," J. Fluid Mech. **253**, 173–209 (1993).

Charney, J. G. and G. R. Flierl, "Oceanic analogies of large scale atmospheric motions 1981," in *Evolution of Physical Oceanography,* edited by B. A. Warren and C. Wunsch (MIT Press, Cambridge, 1981), pp. 504–548.

Dritschel, D. G., "Vortex properties of two-dimensional turbulence," Phys. Fluids A **5**, 984–997 (1993).

Dowling, T. E. and A. P. Ingersoll, "Jupiter's Great Red Spot as a shallow water system," J. Atmos. Sci. **46**, 3256–3278 (1989).

Durran, D., "The third order Adams–Bashforth method: An attractive alternative to leapfrog time differencing," Mon. Weather Rev. **119**, 702–720 (1991).

Farge, M., "Dynamique non-linéare des ondes et des tourbillons dans les équations de Saint-Venant," Thèse de Doctorat d'Etat, Université Paris VI, 1987.

Farge, M. and R. Sadourny, "Wave-vortex dynamics in rotating shallow water," J. Fluid Mech. **206**, 433–462 (1990).

Ford, R., "Gravity wave generation by vortical flows in a rotating frame," Ph.D. thesis, Cambridge University, 1993. Copies available from the author upon request.

Hoskins, B. J., M. E. McIntyre and A. W. Robertson, "On the use and significance of isentropic potential vorticity maps," Q. J. R. Meteorol. Soc. **111**, 877–946 (1985).

Larichev, V. D. and J. C. McWilliams, "Weakly decaying turbulence in an equivalent barotropic model," Phys. Fluids A **3**, 938–950 (1991).

Lighthill, M. J., "On sound generated aerodynamically. I. General theory," Proc. R. Soc. London Ser. A **211**, 564–587 (1952).

MacLow, M-M. and A. P. Ingersoll, "Merging of vortices in the atmosphere of Jupiter: An analysis of voyager images," Icarus **65**, 353–369 (1986).

McWilliams, J. C., "The emergence of isolated coherent vortices in turbulent flow," J. Fluid Mech. **146**, 21–43 (1984).

McWilliams, J. C., "A note on a uniformly valid model spanning the régimes of geostrophic and isotropic, stratified turbulence: Balanced turbulence," J. Atmos. Sci. **42**, 1773–1774 (1985).

Nezlin, M. V. and E. N. Snezhkin, *Rossby Vortices, Spiral Structures, Solitons: Astrophysics and Plasma Physics in Shallow Water Experiments* (Springer-Verlag, Berlin, 1993).

Polvani, L. M., N. J. Zabusky, and G. R. Flierl, "Two-layer geostrophic vortex dynamics. Part 1. Upper layer V-states and merger," J. Fluid Mech. **205**, 215–242 (1989).

Robert, A. J. "The integration of a low order spectral form of the primitive meterological equations," J. Meteorol. Soc. Jpn. **44**, 237–245 (1966).

Santangelo, R., R. Benzi, and B. Legras, "The generation of vortices in high-resolution, two-dimensional decaying turbulence," Phys. Fluids A **1**, 1027 (1989).

Scheidegger, T. E., N. J. Zabusky, and R. B. Pelz, "Effects of compressibility on the dynamics of coherent vortices," Bull. Am. Phys. Soc. **38**, 125 (1993).

Spall, M. A. and J. C. McWilliams, "Rotational and gravitational influences on the degree of balance in the shallow water equations," Geophys. Astrophys. Fluid Dyn. **64**, 1–29 (1992).

Williams, G. P. and T. Yamagata, "Geostrophic regimes, intermediate solitary vortices, and Jovian eddies," J. Atmos. Sci. **41**, 453–478 (1984).

Williams, G. P. and R. J. Wilson, "The stability and genesis of Rossby vortices," J. Atmos. Sci. **45**, 207–241 (1988).

Yavneh, I. and J. C. McWilliams, "Efficient multigrid solutions of the shallow water Balance equations," submitted to J. Comp. Phys. (1993a).

Yavneh, I. and J. C. McWilliams, "Breakdown of the slow manifold in the shallow-water equations," Geophys. Astrophys. Fluid Dyn. (1993b).

Yuan, L., "Statistical equilibrium dynamics in a forced-dissipative f-plane shallow water model," Ph.D. thesis, Princeton University, 1993.

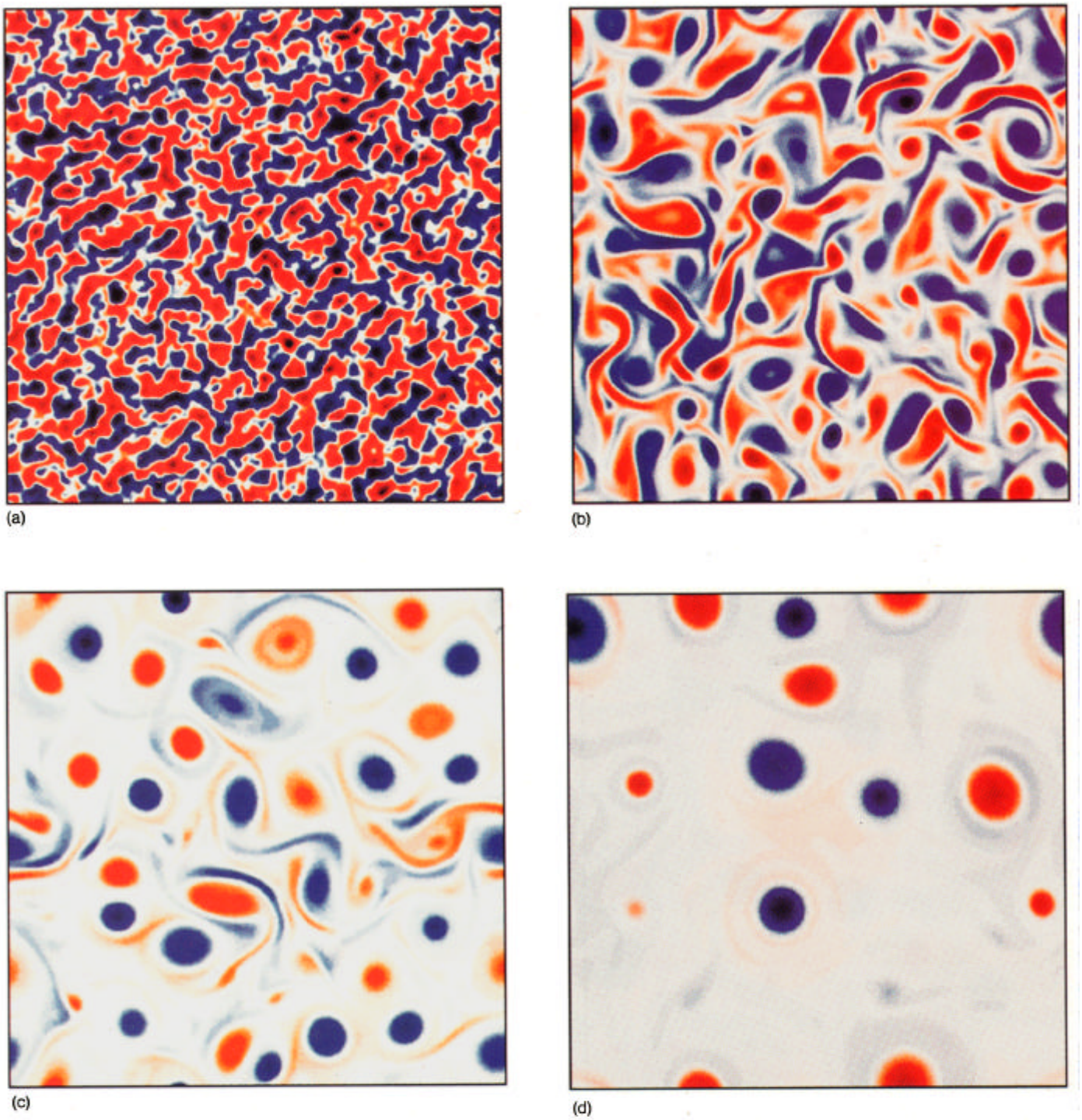

FIG. 8. The vorticity (a) at $t=0$, and at $t=1000$ for runs (b) A, (c) B, and (d) D.

Polvani *et al.* (see page 182)

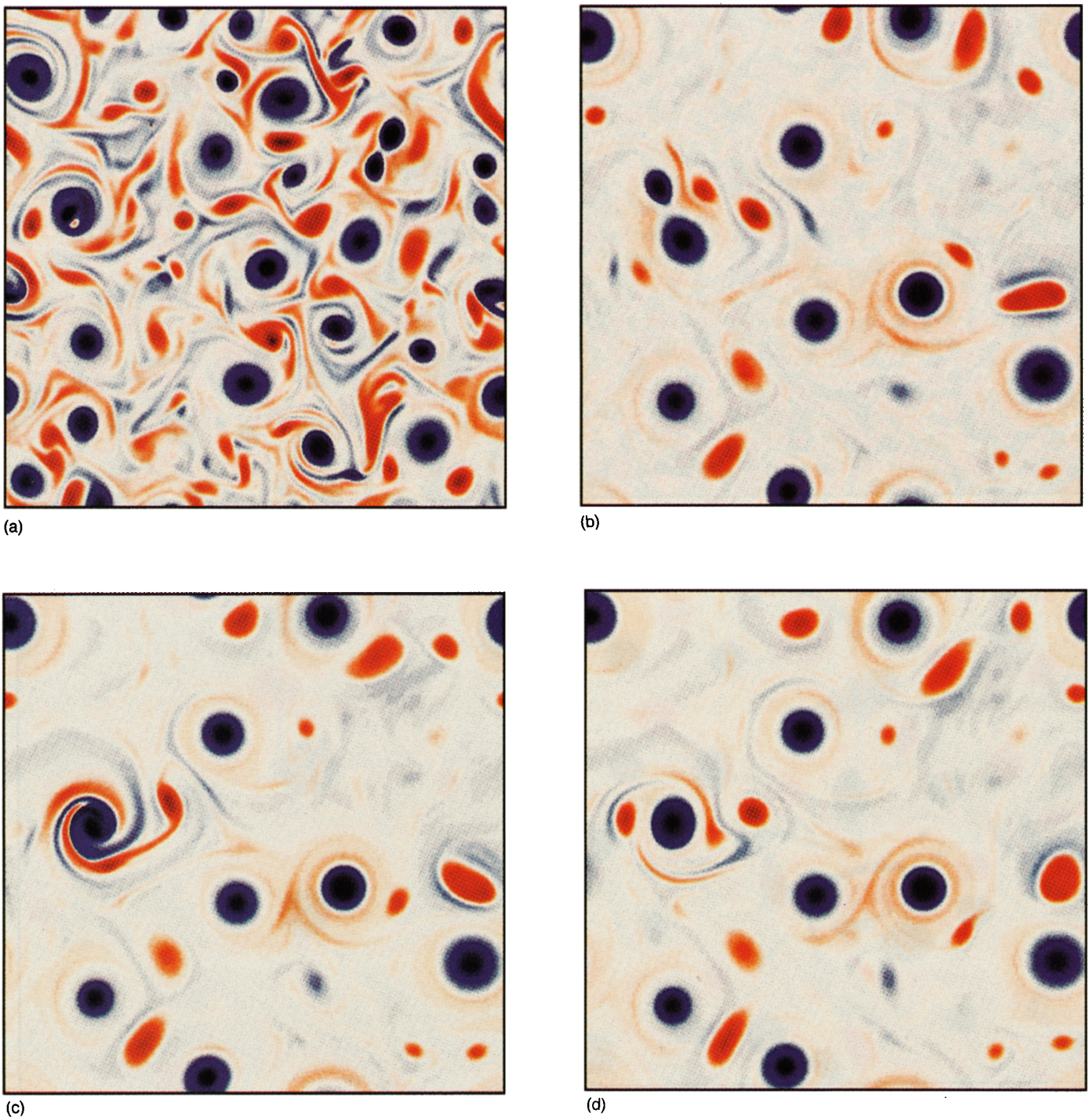

FIG. 12. The vorticity for run G at (a) $t=100$, (b) $t=425$, (c) $t=450$, and (d) $t=475$.

Polvani *et al.* (see page 183)

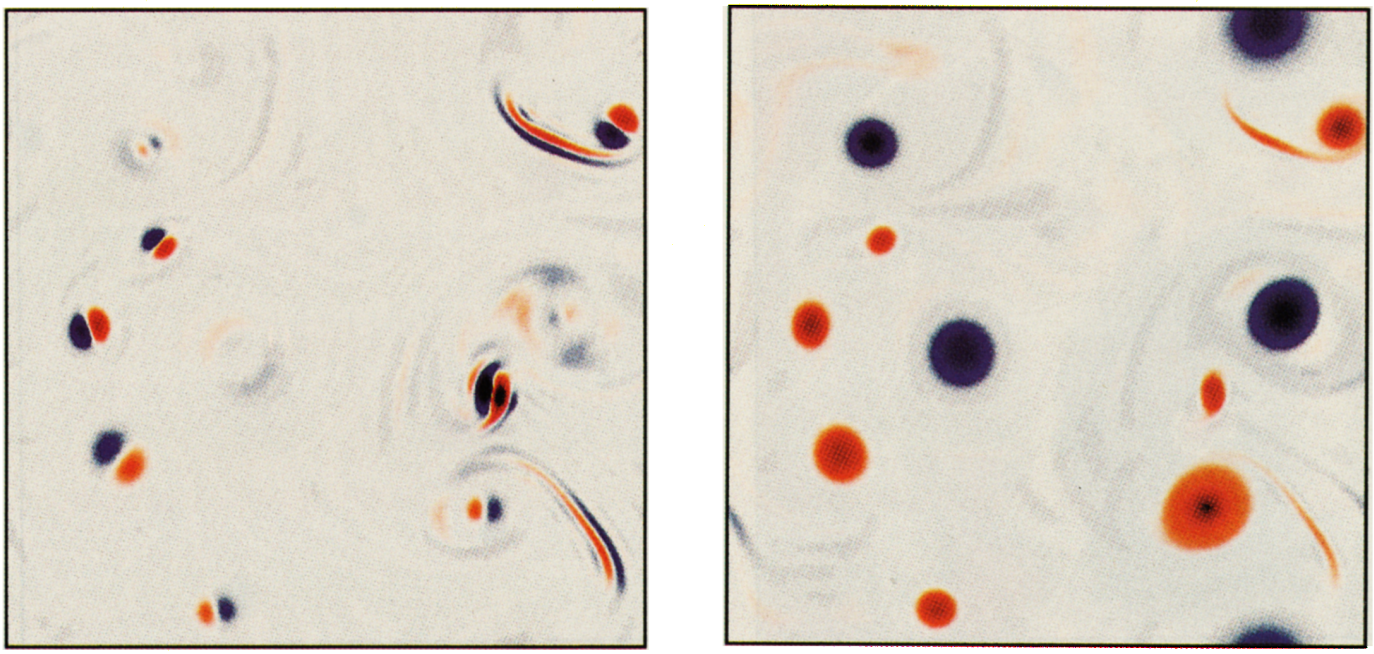

FIG. 14. The fields of (a) $\partial_i \partial_j T_{ij}$ and (b) vorticity for run F at $t=500$.

Polvani *et al.* (see page 184)

PLATE 4

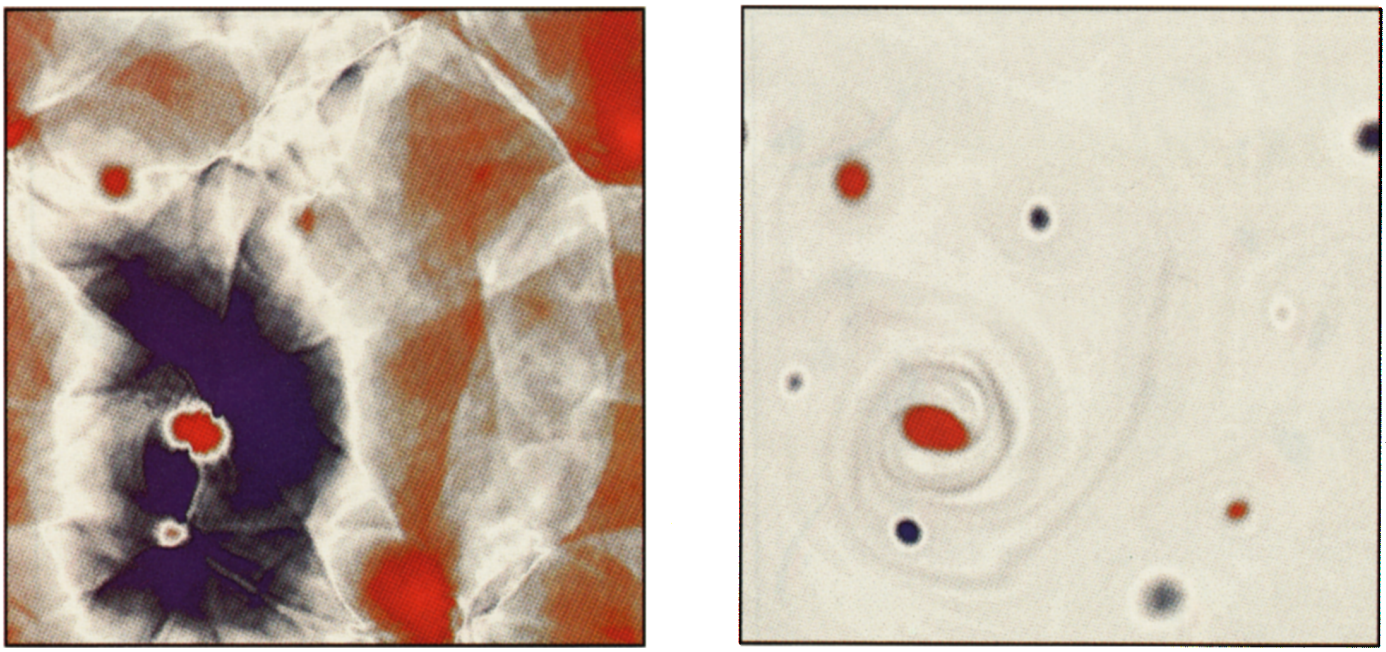

FIG. 15. The (a) height and (b) vorticity fields for run I at $t=1000$.

Polvani *et al.* (see page 184)